NANO LETTERS

2007
Vol. 7, No. 8
2356−2364

Vertically Oriented Ti–Fe–O Nanotube Array Films: Toward a Useful Material Architecture for Solar Spectrum Water Photoelectrolysis

Gopal K. Mor, Haripriya E. Prakasam, Oomman K. Varghese, Karthik Shankar, and Craig A. Grimes*

Department of Electrical Engineering and Materials Research Institute, The Pennsylvania State University, University Park, Pennsylvania 16802

Received April 27, 2007; Revised Manuscript Received May 23, 2007

ABSTRACT

In an effort to obtain a material architecture suitable for high-efficiency visible spectrum water photoelectrolysis, herein we report on the fabrication and visible spectrum (380–650 nm) photoelectrochemical properties of self-aligned, vertically oriented Ti–Fe–O nanotube array films. Ti–Fe metal films of variable composition, iron content ranging from 69% to 3.5%, co-sputtered onto FTO-coated glass are anodized in an ethylene glycol + NH_4F electrolyte. The resulting amorphous samples are annealed in oxygen at 500 °C, resulting in nanotubes composed of a mixed Ti–Fe–O oxide. Some of the iron goes into the titanium lattice substituting titanium ions, and the rest either forms α-Fe_2O_3 crystallites or remains in the amorphous state. Depending upon the Fe content, the band gap of the resulting films ranges from about 380 to 570 nm. The Ti–Fe oxide nanotube array films are utilized in solar spectrum water photoelectrolysis, demonstrating 2 mA/cm^2 under AM 1.5 illumination with a sustained, time–energy normalized hydrogen evolution rate by water splitting of 7.1 mL/W·hr in a 1 M KOH solution with a platinum counter electrode under an applied bias of 0.7 V. The surface morphology, structure, elemental analysis, optical, and photoelectrochemical properties of the Ti–Fe oxide nanotube array films are considered.

Prospects for large-scale use of hydrogen as a portable energy carrier are predicated upon a clean and sustainable method of its production. In 1972, Fujishima and Honda[1] reported the use of a TiO_2 semiconductor photoanode for water photoelectrolysis, using solar energy to split water into hydrogen and oxygen. For sustained water splitting to occur, several semiconductor properties such as band gap, flat band potential, and corrosion stability must be simultaneously optimized.[2,3] Hematite, or α-Fe_2O_3, is a n-type semiconductor with a ∼2.2 eV band gap that is sufficiently large enough for water splitting but small enough to collect a significant fraction, ≈40%, of solar spectrum energy. However iron oxide suffers from low electron mobility, generally in the range of 0.01 cm^2/V·s [4] to 0.1 cm^2/V·s [5], resulting in rapid electron−hole recombination, and an insufficiently negative flat band potential as needed for spontaneous water splitting.[6] Therefore, α-Fe_2O_3 solar spectrum photoconversion efficiencies reported to date are far from the theoretical maximum value of 12.9% for a material of this band gap.[7]

TiO_2 is a n-type semiconductor exhibiting excellent charge-transfer properties and photochemical stability; furthermore, its band gap includes the redox potential for the H_2O/•OH reaction, allowing photogeneration of oxygen through water splitting.[8] However the band gap of TiO_2, ∼3.0 eV for rutile and 3.2 eV for anatase, limits its activation to UV radiation, which accounts for only ≈5% of solar spectrum energy. Efforts to shift the band gap of TiO_2 while maintaining its excellent charge-transfer properties and photocorrosion stability have primarily focused on metal doping.[9−14] Metal ion doping introduces mid-gap energy levels; however, beyond a minimal concentration, the metal ions serve as recombination centers for the photogenerated electron−hole pairs. Hence although iron doping of TiO_2 has successfully extended its photoresponse to visible light,[10,15−18] the resulting materials have demonstrated, at best, mixed photocatalytic activities.

In addition to the band gap, the material architecture of a semiconductor photoanode plays a critical role in determining the resultant photoconversion efficiencies. Recombination in low mobility materials can be minimized by decreasing the relevant architectural feature size(s) to less than the minority carrier diffusion length; for α-Fe_2O_3, the hole diffusion length is 2−4 nm.[19] This is of particular interest as the authors have recently reported fabrication of vertically oriented, highly ordered TiO_2 nanotube arrays from 200 nm to 720 μm length,[20−22] having wall thicknesses of ≈4 nm.[23] Highly

* Corresponding author. E-mail: cgrimes@engr.psu.edu.

10.1021/nl0710046 CCC: $37.00
Published on Web 07/03/2007

Table 1. Assigned Sample Name, Iron and Titanium Target Powers, and Corresponding Sputter Rates, Substrate Temperature, and Thickness of Resulting Ti−Fe Film, Ti−Fe Film Composition

sample	Fe target power (W)/sputter rate (nm/s)	Ti target power (W)/sputter rate (nm/s)	substrate temp °C	film thickness (nm)	film composition	crystallinity of metal starting film
69	300/5.5	100/2.5	350	400	69% Fe-31% Ti	crystalline
44	300/5.5	300/7.0	350	1000	44% Fe-56% Ti	crystalline
37	250/4.1	300/7.0	350	500	37% Fe-63% Ti	amorphous
26	200/2.5	300/7.0	350	400	26% Fe-74% Ti	amorphous
20	150/1.3	300/7.0	400	750	20% Fe-80% Ti	amorphous
6.6a	100/0.5	300/7.0	400	750	6.6% Fe-93.4% Ti	crystalline
6.6b	100/0.5	300/7.0	400	1500	6.6% Fe-93.4% Ti	crystalline
3.5	50/0.25	300/7.0	400	750	3.5% Fe-96.5% Ti	crystalline

ordered vertically oriented TiO_2 nanotube arrays fabricated by anodization of titanium at constant voltage constitute a material architecture that offers a large internal surface area without a concomitant decrease in geometric and structural order. The precisely oriented nature of the crystalline (after annealing) nanotube arrays makes them excellent electron percolation pathways for vectorial charge transfer between interfaces.[24] Such a material architecture in α-Fe_2O_3 offers the intriguing prospect of efficient charge transfer in a material well suited for capturing solar spectrum energy. Where the use of vertically oriented titania nanotube arrays have been studied, an extraordinary enhancement of the extant TiO_2 properties has been found.[25−31]

The authors have reported three synthesis generations of the vertically oriented TiO_2 nanotube arrays made by titanium anodization at different constant voltages and their application to water photoelectrolysis.[21,32,33] The first generation of titania nanotube arrays, reported in 2001 by Gong and coworkers,[20] used an aqueous HF-based electrolyte in which nanotube arrays were grown to a length of about 500 nm.[33−35] In the second generation, nanotube array lengths were increased to about 7 μm by control of the anodization electrolyte pH.[36−38] In the third generation, TiO_2 nanotube arrays up to $\approx$1.5 mm (1500 μm) in length have been obtained by using various nonaqueous polar organic electrolytes, including formamide, dimethylsulfoxide, DMSO, and ethylene glycol.[21−23,39,40] TiO_2 nanotube arrays several tens of micrometers long demonstrate a photoconversion efficiency of 16.5% under UV illumination, 320−400 nm, with an intensity of 100 mW/cm^2.[23,40]

The hypothesis underlying our current effort is that we could achieve high solar energy photoelectrochemical properties if, in one material architecture, we could combine the charge transport and photocorrosion properties of the TiO_2 nanotubes with the band gap of α-Fe_2O_3. To that end, the authors recently reported fabrication of highly ordered nanoporous α-Fe_2O_3 by anodic oxidation of iron foil in NH_4F + ethylene glycol electrolyte.[41,42] Because both Ti and Fe can be anodized in a fluoride ion containing ethylene glycol solution, the possibility exists for obtaining highly ordered, vertically oriented Ti−Fe oxide nanotube arrays, the material architecture we desire for application to water photoelectrolysis, by anodization of Ti−Fe metal films. That said, herein we report on anodic oxidation of Ti−Fe metal films, with iron content ranging from 69% to 3.5%, to fabricate Ti−Fe−O films possessing a vertically oriented, nanotube array structure. Surface morphology, structural characterization identifying phases, optical measurements exhibiting absorbance in visible range, X-ray photoelectron spectroscopy determining chemical states of Fe and Ti, and photoelectrochemical behavior under simulated solar light (AM 1.5) of these Ti−Fe−O nanotube array films have been studied and are discussed herein.

Experimental. Ti−Fe metal films were deposited on fluorine-doped tin oxide (FTO) coated glass substrates by simultaneous co-sputtering from titanium and iron targets. The substrate temperature was maintained at 350−400 °C. Details of sputtering conditions, the resulting thickness of the Ti−Fe metal films, and their crystallinity are given in Table 1. The metal films of high titanium or high iron concentration are crystalline, with the former a hexagonal titanium lattice and the latter a cubic iron lattice. Films with moderate levels of iron were amorphous. Irrespective of the crystallinity of the starting film, the anodized films were amorphous, with a very thin residual metal layer underneath. Distinct nanotube arrays were formed from samples having iron concentrations less than about 70%. Films of higher Fe content, up to 100% Fe, were fabricated and characterized; however, because they showed significantly diminished photoelectrochemical properties they are not considered herein. We consider Ti:Fe metal films in the ratios 31:69, 56:44, 63:37, 74:26, 80:20, 93.4:6.6, and 96.5:3.5 as determined from the relative sputtering rates, with identifying sample numbers given by the Fe content. A Tencor profilometer was used to determine sputtered film thickness.

Anodization of the Ti−Fe films was performed at a constant voltage of 30 V in ethylene glycol containing 0.3 wt % NH_4F and 2.0 vol % deionized water. The amorphous as-anodized samples were crystallized by oxygen annealing at 500 °C for 2 h. Sample morphology was studied using a JEOL JSM-6300 field emission scanning electron microscope (FESEM) and high-resolution transmission electron microscope (HRTEM, JEOL 2010F). The compositional analysis of the Ti−Fe−O phases in the annealed samples were investigated using glancing angle X-ray diffraction (GAXRD). The X-ray photoelectron spectroscopy (XPS) experiments were performed on the Ti−Fe−O films using a Kratos Axis Ultra spectrometer with an Al anode (Al KR: 1486.6 eV). The anode voltage and current were 14 keV and 20 mA, respectively. Photoelectrons were collected in

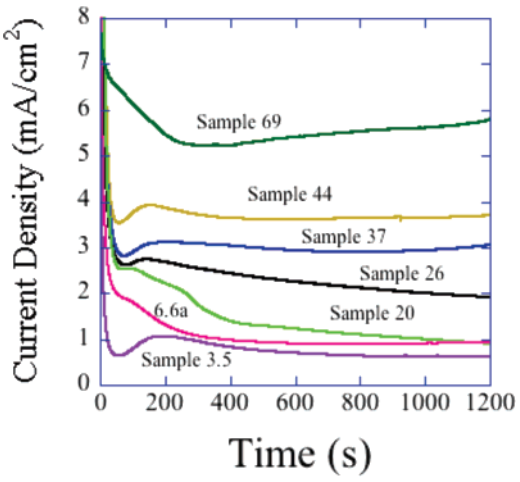

Figure 1. Current−time behavior during anodization of Ti−Fe films, see Table 1, at 30 V in an ethylene glycol electrolyte containing 0.3 wt % NH_4F and 2.0 vol % deionized water.

hybrid mode over an analysis area of about 1.5 mm^2, with the plane of the sample surface normal to the analyzer entrance. Spectra were charge referenced to C 1s at 285 eV.

Optical characterization of the films was performed using a Cary UV−vis spectrophotometer. The photoelectrochemical properties were investigated using a three-electrode configuration with a Ti−Fe−O photoanode as the working electrode, saturated Ag/AgCl as a reference, and platinum foil as a counter electrode. A 1.0 M NaOH solution was used as the electrolyte. A scanning potentiostat (CH Instruments, model CHI 600B) was used to measure dark and illuminated current at a scan rate of 10 mV/s. Sunlight was simulated with a 300 W xenon lamp (Spectra Physics) and AM 1.5 filter (Oriel). The light intensity was set using a NREL calibrated crystalline silicon solar cell, equivalent to AM 1.5 light at 100 mW/cm^2. Incident photon-to-current conversion efficiency (IPCE) measurements were performed with the spectral irradiance of the light from the 300 W xenon lamp, integrated with a parabolic reflector, passing through an AM 1.5 filter and monochromator determined using an Oriel-calibrated silicon photodiode.

Figure 1 compares the real-time constant voltage anodization behavior of the Ti−Fe films, with the samples identified by their iron content, anodized at 30 V in EG + 0.3 wt % NH_4F + 2.0% deionized water; a systematic variation in anodization behavior is seen with decreasing Fe content. The sharp drop in the anodization current in the first 100 s is due to the formation of an initial electrically insulating oxide layer, followed by an increase in the current due to oxide pitting by the fluoride ions. The current then gradually decreases to plateau at a steady-state value corresponding to maximum nanotube length. Illustrative top, cross-sectional, and bottom-side FESEM images of samples 44, 20, and 3.5 are shown in Figure 2. TiO_2 nanotube array formation by anodization in aqueous electrolytes is purely a subtractive process; one starts with a titanium film of thickness X and achieves a nanotube array of thickness less than X.[20,34] In contrast, using an ethylene glycol electrolyte, one can begin with a Ti film of thickness X and achieve a nanotube array of thickness greater than X, with material removed from the pores going into wall formation. Nanotube arrays obtained from constant voltage anodization of Ti foil in ethylene glycol containing 0.3 wt % NH_4F and 2.0 vol % deionized water have shown lengths up to 3.5× greater than the starting Ti foil thickness.[21,22] A similar effect is seen for anodization of the Ti−Fe films of higher Ti content. The nanotube lengths obtained from sample 44 films are close to the starting film thickness, whereas for sample 3.5, the resulting nanotubes are nearly twice the length of the starting metal film thickness.

We note the addition of water to the ethylene glycol electrolyte as a critical ingredient, with water the usual source of oxygen in polar organic electrolytes.[43] While the exact mechanism by which water contributes oxygen to an anodic oxide film is not well understood, evidence suggests hydroxyl ion injection from the electrolyte into the anodic oxide film.[43,44] When too much water is present, hydroxyl ions are injected into the oxide layer, sufficiently affecting the structure to impede ion transport though the barrier layer, which is necessary for further movement of the metal−oxide interface into the metal.[45] When too little water is present, the difficulty in extracting oxygen and/or hydroxyl ions from the solution limits the rate of the oxide film growth, and the barrier oxide layer exhibits increased ionic conductivity caused by the nonstoichiometry induced by the reduced hydroxyl ion availability to the oxide.[46] The amount of hydroxyl ion injection is dependent on the solvent structure; ethylene glycol has a clearly pronounced spatial net of hydrogen bonds. When the solvent structure provides an environment in which titanium ions at the oxide surface bond to surface oxygen ions, minimal hydroxyl ion injection occurs and ionic transport through the barrier layer is relatively rapid. The electrolyte conductivity also plays a role in controlling nanotube array growth. Ethylene glycol containing 2.0% water and 0.3% NH_4F has a conductivity 460 μS/cm. The total applied anodization voltage is the sum of the potential difference at the metal−oxide interface, the potential drop across the oxide, the potential difference at the oxide−electrolyte interface, and the potential drop across the electrolyte, which is non-negligible for ethylene glycol-based electrolytes. TiO_2 nanotube arrays can be achieved at 30−40 V in ethylene glycol baths, whereas in fluoride ion containing aqueous baths, nanotube arrays are obtained only between 10 and 15 V.[34]

Film Structure. As-anodized Ti−Fe−O nanotube films are amorphous, partially crystallized by annealing in oxygen atmosphere at 500 °C for 2 h with a ramp up and down rate of 1 °C /min. GAXRD patterns of the annealed films are seen in Figure 3. All studies on TiO_2 nanotube array films made by anodization have indicated the tubes to be anatase, fixed atop a rutile base.[47] The Ti−Fe−O samples with low iron concentrations show the presence of anatase phase; sample 3.5 is largely anatase with a dominant (110) plane and a small amount of rutile. The anatase phase disappears at higher iron concentrations (see the patterns of samples 20 and 37). The presence of the rutile peak is evident in samples 6.6 and 20, which is consistent with the fact that

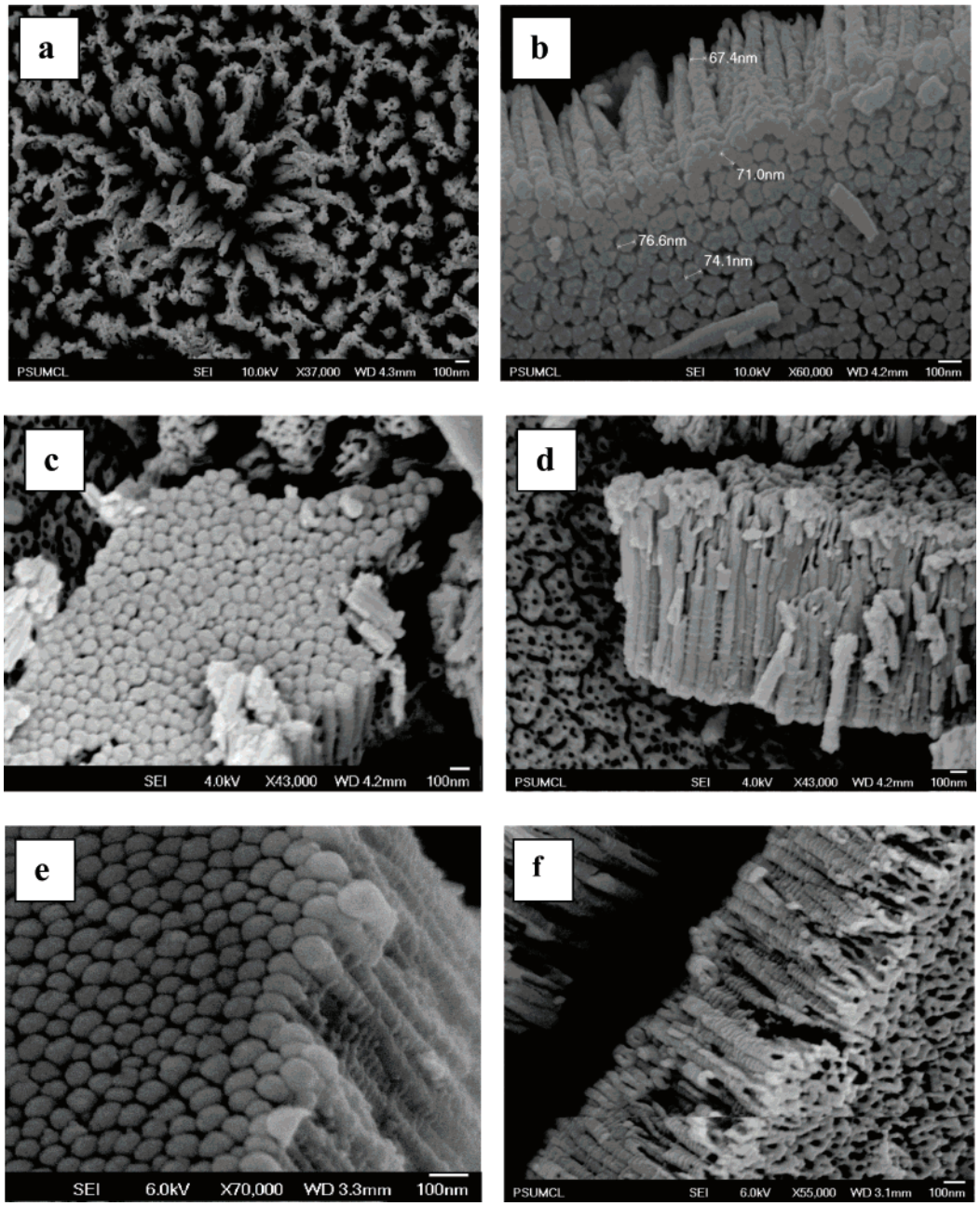

Figure 2. Illustrative FESEM images of Ti−Fe−O nanotube array samples. Sample 44, top surface and lateral view are seen in (a) and (b). Sample 20, image of tube bottom (c) and lateral view (d). Sample 3.5, image of tube bottom (e) and lateral view (f).

low amounts of iron in titania aid rutile formation.[48−50] The predominant (104) plane of α-Fe_2O_3 coincides with the second intense plane of FTO, used as the conductive layer on the glass substrate, and its subsequent two less-intense planes, (110) and (116), appear at $2\theta = 35.6$ and 54.1, respectively. The XRD pattern of sample 26 is omitted from Figure 3 because of its relatively weak peaks. In sample 37, the proportion of rutile increases slightly, and anatase is almost negligible. In general, samples 20 and 37 showed poor crystallinity, sample 44 showed pseudobrookite phase, while sample 69 showed hematite phase. In general, it appears that the presence of iron inside the TiO_2 matrix degrades the crystallization process because the proportion of rutile does not increase with decreasing amounts of anatase, an outcome possibly due to the fixed 500 °C annealing temperature. However, higher annealing temperatures spoil the FTO−TiFeO interface, resulting in samples of high series resistance demonstrating essentially nil photoelectrochemical properties.

The crystalline nature of the nanotube walls is critical to applications involving light absorption, electrical carrier generation, and carrier transport, therefore the crystalline nature of the nanotube walls were studied using HRTEM. Sample 20, with moderate iron doping, was used for the study. TEM studies confirmed the relatively poor crystallinity of samples annealed at 500 °C, hence further studies were conducted on a sample 20 annealed at 600 °C for 2 h in oxygen. As seen in Figure 2, and as described in our earlier articles on TiO_2 nanotube arrays formed in HF aqueous electrolytes,[20,34] the nanotube morphology appears as a column of stacked torus (doughnut) shaped rings as seen in

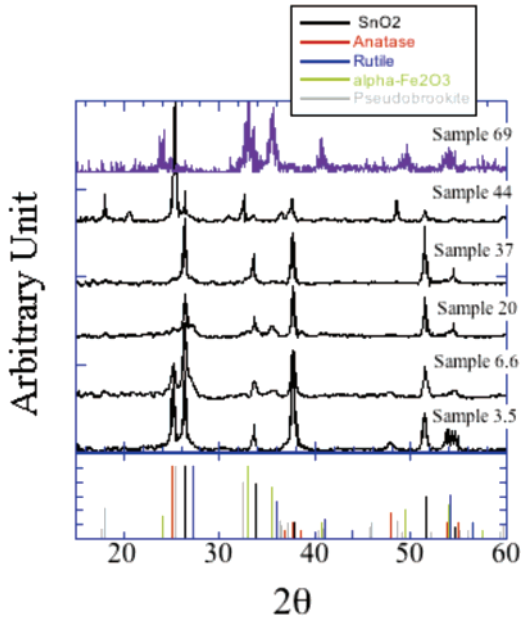

Figure 3. GAXRD patterns of Ti−Fe−O nanotube array samples annealed at 500 °C in dry oxygen for 2 h, see Table 1 for fabrication details. Standard patterns for anatase, rutile, pseudobrookite, α-Fe_2O_3 (hematite), and tin oxide (substrate) are shown for phase identification.

the TEM image of Figure 4a. A selected area electron diffraction (SAED) pattern from the corresponding region is shown in Figure 4b. Although the pattern shows mainly rutile phase, reflections from hematite phase also can be seen. Figure 5a shows a HRTEM image of a nanotube wall, with the polycrystalline nature evident from the figure. The crystallites have a wide size distribution. The crystallite marked R has a rutile structure, the lattice image of which is given in the upper left inset. A fast Fourier transform (FFT) of regions R and H are given in Figure 5b,c, indicating the presence of rutile and hematite phases in the respective regions.

To find the distribution of iron within the nanotube walls, an energy dispersive X-ray spectroscopy (EDS) line scan was performed via scanning transmission electron microscopy (STEM), see Figure 6. The intensity of both the TiK_α and FeK_α lines are maximum at the center of the wall due to its torus shape. Despite the presence of isolated hematite crystallites, a more or less uniform distribution of iron relative to the titanium can be seen across the wall. STEM line scans were performed across a number of walls, and while the average relative intensity of the TiK_α and FeK_α lines varied from wall to wall, the relative distribution across a single wall remained uniform. It appears that some of the iron goes into the titanium lattice substituting titanium ions, and the rest either forms hematite crystallites or remains in the amorphous state.

Crystallization of the as-anodized amorphous nanotubes takes place through nucleation and growth.[47] Hence, a sufficiently high temperature and appropriate duration are needed for the complete transformation of the amorphous phase into crystalline. The removal of the amorphous phase is critical for effective device application; however, even after annealing at 600 °C, sample 20 showed the presence of amorphous phase. HRTEM studies indicate that rutile and hematite phases are formed in separate events depending upon the temperature and nature of the nucleation sites. In general, the nanotubes of moderate iron concentration consist mainly of rutile phase with hematite crystallites randomly distributed.

XPS survey spectra (not shown) reveal the Ti−Fe oxide films to contain Ti, O, Fe, and C. The photoelectron peaks for Ti 2p appear clearly at a binding energy (E_b) of 458 eV, O 1s at E_b = 530 eV, and Fe 2p at E_b = 711 eV. The XPS peak for C 1s at E_b = 285 eV was observed due to adventitious carbon from sample fabrication and/or the XPS instruments itself. Figure 7a is high-resolution Ti 2p region spectra taken on the surface of samples 44, 26, and 3.5 showing the presence of the main doublet composed of two symmetrical peaks at $E_b(Ti\ 2p_{3/2})$ = 458.8 eV and $E_b(Ti\ 2p_{1/2})$ = 464.5 eV, assigned to Ti^{4+} in the spectrum of Ti−Fe oxide film.[50] A high-resolution spectrum of the Fe 2p region for samples 44, 26, and 3.5 are shown in Figure 7b. The spectrum indicates the existence of doublet Fe $2p_{3/2}$ and Fe $2p_{1/2}$ and their corresponding satellites that are characteristic of Fe_2O_3.[51−54] The intensity of these satellite features diminishes significantly in sample 3.5. No component related to zero valent Fe and Ti can be extracted. It is not appropriate to determine the Ti/Fe atomic ratio using XPS because the surface morphology of the film is nanotubular, or porous, and iron-based compounds are difficult to accurately predict using XPS,[55] as sophisticated curve fitting is required with extensive analysis.

Figure 8a is a photograph showing the color variation in the samples as a function of iron content. Figure 8b shows the absorbance of the annealed samples; as expected, the absorbance edge shows a red-shift with increasing Fe content. According to the band gap structure of TiO_2, the π bonding orbit and π^* antibonding orbit formed by the t_{2g} orbit in Ti^{4+} ions, and the pπ orbit in the O^{2-} of TiO_2 crystal lattice are, respectively, the valence band and conduction band. A new energy band is formed in the TiO_2 band gap when Fe^{3+} ions are partly substituted for the Ti^{4+} ions. The mixing of the Ti(d) orbit of Ti oxide and Fe 3d orbit is essential to decreasing the energy gap between Ti(d) and O(p) orbitals of Ti oxide.

Photoelectrochemical Properties. Figure 9 shows current versus voltage characteristics for the nanotubular Ti−Fe−O electrodes under dark and simulated sunlight in 1.0 M NaOH. The electrodes show n-type behavior, i.e., positive photocurrents at anodic potentials. The dark current in each case is negligible up to 0.65 V (vs Ag/AgCl) beyond which the dark currents for water oxidation dominate, therefore no photocurrent saturation is observed. A metal-coated glass substrate was placed adjacent to translucent sample 6.6b, reflecting the transmitted light back into the sample. This method increased the photocurrent from 1.50 to 2.0 mA/cm^2 at 0.65 V (vs Ag/AgCl). For comparison, the photocurrent of a pure nanoporous α-Fe_2O_3 film 1.5 μm thick on FTO glass is also shown in Figure 9, prepared by anodic oxidation of an iron film at 30 V in ethylene glycol

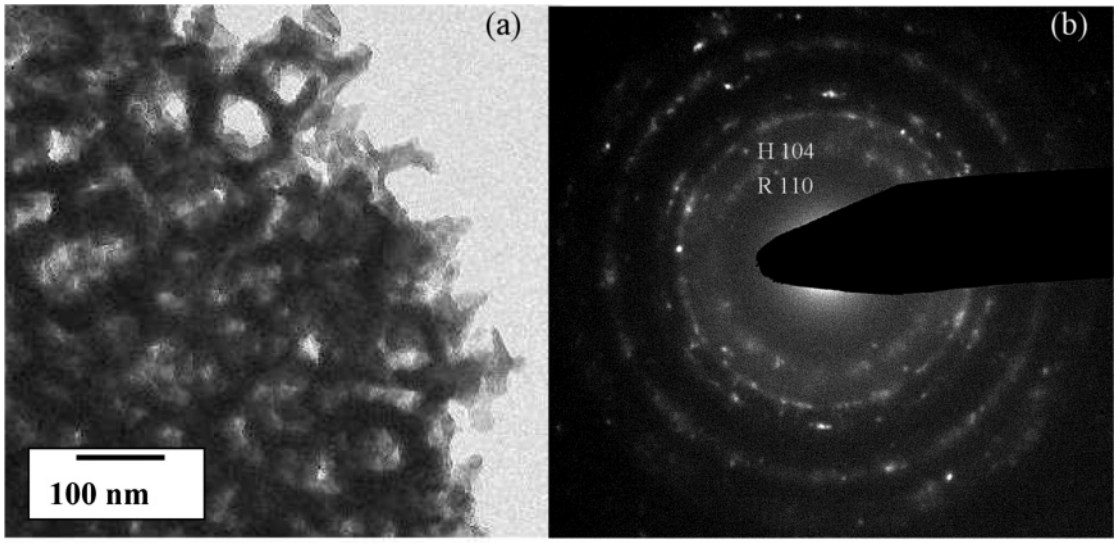

Figure 4. (a) TEM image of sample 20 annealed at 600 °C, and (b) selected area diffraction pattern (H, hematite and R, rutile).

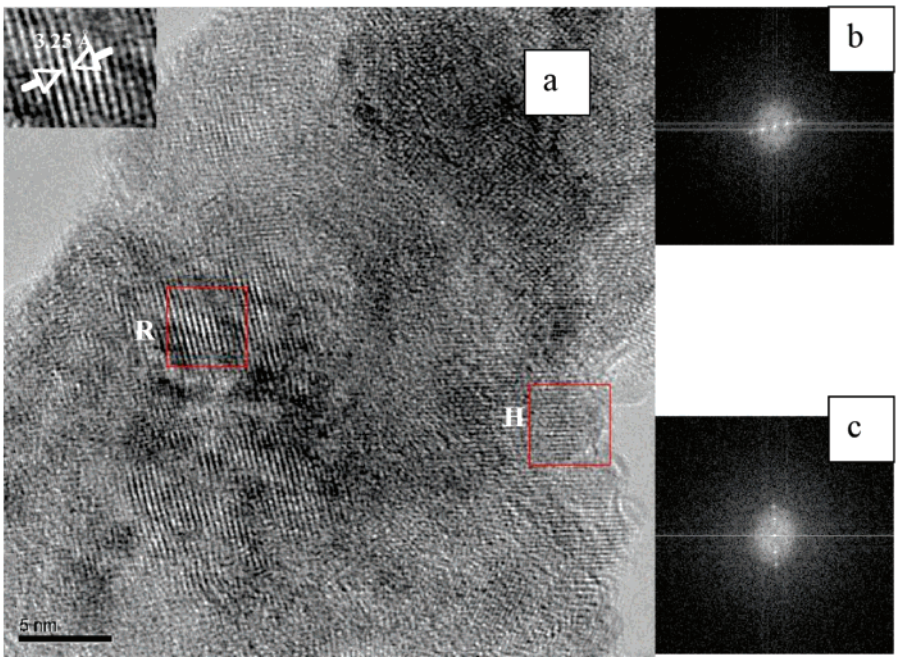

Figure 5. (a) HRTEM image of a nanotube wall (sample 20 annealed at 600 °C) showing rutile (region R) and hematite (region H) crystallites with the lattice image of region R given in the upper-left inset; (b) FFT of region R showing a predominant 110 plane, and (c) FFT of region H showing a predominant 104 plane.

containing 0.3 wt % NH_4F and 0.5% deionized water. Even though this film strongly absorbs visible light, the poor electron mobility results in a maximum photocurrent of 20−25 μA/cm^2 at 0.4 V (vs Ag/AgCl). The highest photocurrent is exhibited by sample 6.6, while the lowest photocurrent is demonstrated by sample 3.5. It appears that minimal levels of Fe^{3+} ions act as trap sites, while significant amounts of Fe^{3+} ions increase the recombination rate of the photogenerated electron−hole pairs. We note sample 44 does not comply with this trend, possibly due to the presence of the pseudobrookite phase, $FeTiO_5$.

Two electrode measurements were performed to determine the photoconversion and light energy to chemical energy conversion efficiency. Photoconversion efficiency η is calculated as:

$$\eta(\%) = j_p[(1.23 - V)/I_0] \times 100 \quad (1)$$

where j_p is the photocurrent density (mA/cm^2), I_0 is the intensity of incident light (mW/cm^2), and V is the potential applied between the anode (Ti−Fe−O sample) and cathode (platinum). The efficiency of mirror-backed sample 6.6b was determined to be 1.2%.

Hydrogen generation experiments were done at constant voltage bias (1 M KOH solution) at an applied bias of 0.7 V. Under AM 1.5 100 mW/cm^2 illumination, sample 6.6b

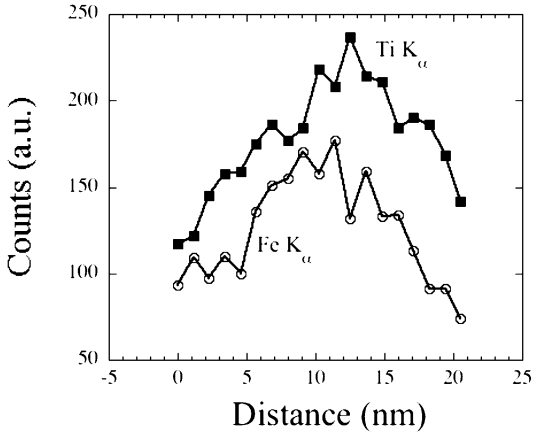

Figure 6. EDS line scan profile across nanotube wall (from region similar to that shown in Figure 5a)

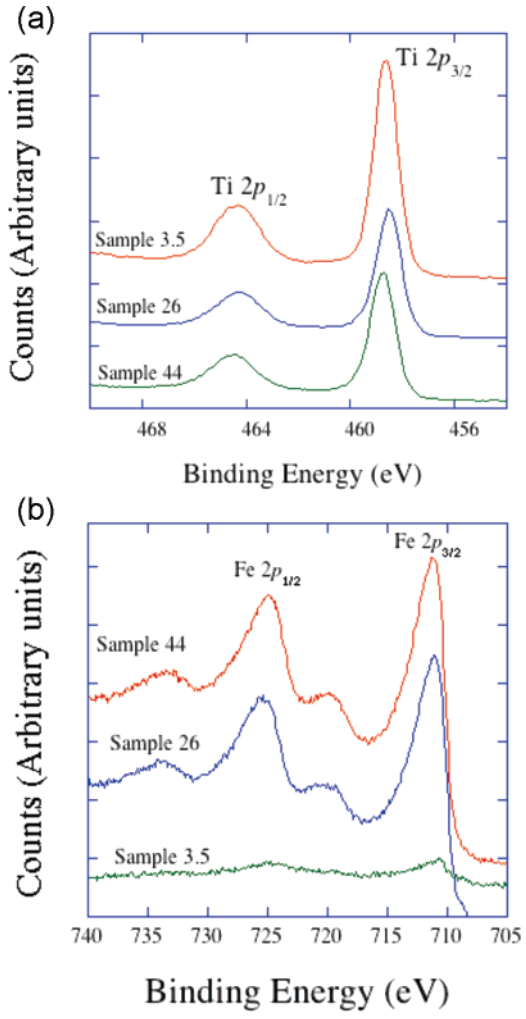

Figure 7. High-resolution XPS spectra from the surface of annealed samples 44, 26, and 3.5: (a) Ti 2p and (b) Fe 2p.

demonstrated a sustained, time-energy normalized hydrogen evolution rate by water splitting of 7.1 mL/W•h. The water splitting reaction was confirmed by the 2:1 ratio of evolved hydrogen to oxygen, as confirmed by a gas chromatograph (SRI, model 8610C). No degradation in sample performance was observed under illumination over a course of several days.

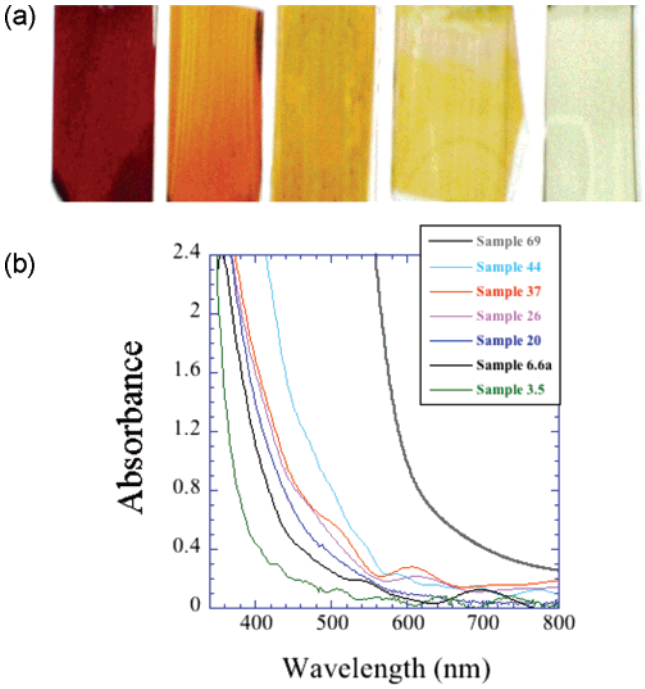

Figure 8. (a) From left, a 1.5 μm α-Fe_2O_3 film, samples 44, 20, 6.6a, and 3.5. (b) Absorbance spectra of 500 °C annealed Ti−Fe−O nanotube array films, see Table 1.

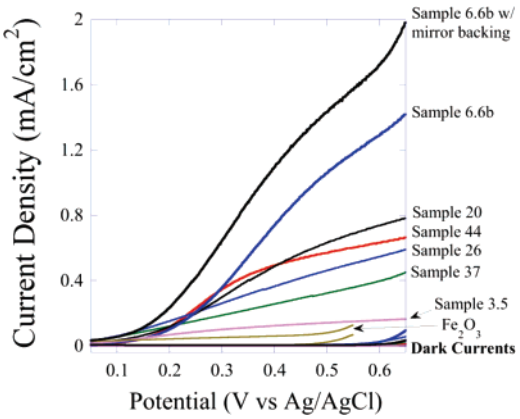

Figure 9. Photocurrent density vs potential in 1 M NaOH solution for annealed Ti−Fe−O nanotube array samples, and α-Fe_2O_3 nanoporous film, under AM 1.5 (100 mW/cm^2) illumination. Dark currents are also shown for each sample.

Steady-state wavelength-specific photocurrents were measured for the Ti−Fe−O films in a two-electrode arrangement at different applied voltages. Incident photon-to-current efficiencies (IPCE) are calculated using the following equation:

$$\text{IPCE} = \frac{(1240\ \text{eV·nm})(\text{photocurrent density}\ \mu\text{A/cm}^2)}{(\lambda\ \text{nm})(\text{irradiance}\ \mu\text{W/cm}^2)} \quad (2)$$

Dividing the IPCE by the fraction of incident photons absorbed at each wavelength gives the absorbed photon-to-current efficiency (APCE).[56] Various factors including nanotube length and Fe composition factor into APCE calculation through the absorbance A, as shown below:

$$\mathrm{APCE} = \frac{\mathrm{IPCE}}{1 - 10^{-A}} \qquad (3)$$

Figure 10a,b shows APCE values corresponding to two applied voltages, 0.5 and 0.7 V; APCE values are appreciable only in the visible range from 400 to 600 nm.

Energy level band diagrams indicate electrons photogenerated in α-Fe_2O_3 cannot transfer to the titania conduction band without an applied bias. Because the redox potential for the H_2O/•OH reaction for oxygen evolution is above the valence band of α-Fe_2O_3 in 1M NaOH electrolyte (pH = 14) and the thickness of the α-Fe_2O_3 crystallites is comparable to the hole diffusion length, application of a small positive bias can be used to separate the photogenerated electrons and holes. As shown in Figure 10, APCE values of the films decrease as we move below 400 nm toward the UV region, possibly due to the Fe^{3+} ions of the α-Fe_2O_3 and iron incorporated TiO_2 crystallites becoming Fe^{2+} as associated with oxygen vacancy defects. Because of this, the position of the valence band at solid−electrolyte shifts upward, crossing the redox potential of the H_2O/•OH reaction inhibiting hole transfer and leading to increased recombination.

Conclusions. We report on a novel method for the fabrication of films comprised of vertically oriented Ti−Fe−O nanotube arrays on FTO-coated glass substrates by anodic oxidation of Ti−Fe metal films in an ethylene glycol + NH_4F solvent. Annealing of the initially amorphous films resulted in some of the iron substituting for titanium ions in the titanium lattice and the rest either forming α-Fe_2O_3 crystallites or remaining in the amorphous state. Low Fe content samples demonstrated anatase phase with annealing, moving to rutile phase as the Fe content in the samples increased.

The photoconversion efficiency of TiO_2 nanotube arrays under UV illumination are notable, 16.5% under 320−400 nm band illumination (100 mW/cm^2). UV light, however, accounts for only a small fraction of the solar spectrum energy, hence our motivation in fabricating Ti−Fe−O nanotube arrays. We obtain a photocurrent of 2 mA/cm^2 under AM 1.5 for iron oxide related materials, a value second only to that recently reported by Gratzel of 2.2 mA/cm^2.[57] More importantly, should we be able to reduce the nanotube wall thickness to less than the minority carrier diffusion length, ≈2−4 nm, we would expect dramatically improved photocurrents. However, while the wall thicknesses of TiO_2 nanotubes formed in aqueous-based electrolytes containing fluoride ions can be controlled through the anodization bath temperature,[58] no such temperature-dependent effect was found in this study. Over the various sample compositions, the wall thickness of the Ti−Fe−O nanotubes held constant at ≈22 nm independently of anodization bath temperature (0−50 °C).

Future efforts will focus on adjustment of the electrolyte bath chemistry to see if thin-wall Ti−Fe−O nanotubes can be achieved, that is to say, having a wall thickness comparable to the hole diffusion length in α-Fe_2O_3. The Ti−Fe−O material architecture demonstrates properties useful for hydrogen generation by water photoelectrolysis and, more importantly, we believe the general nanotube array synthesis technique can be extended to other binary or ternary oxide compositions of interest for water photoelectrolysis.

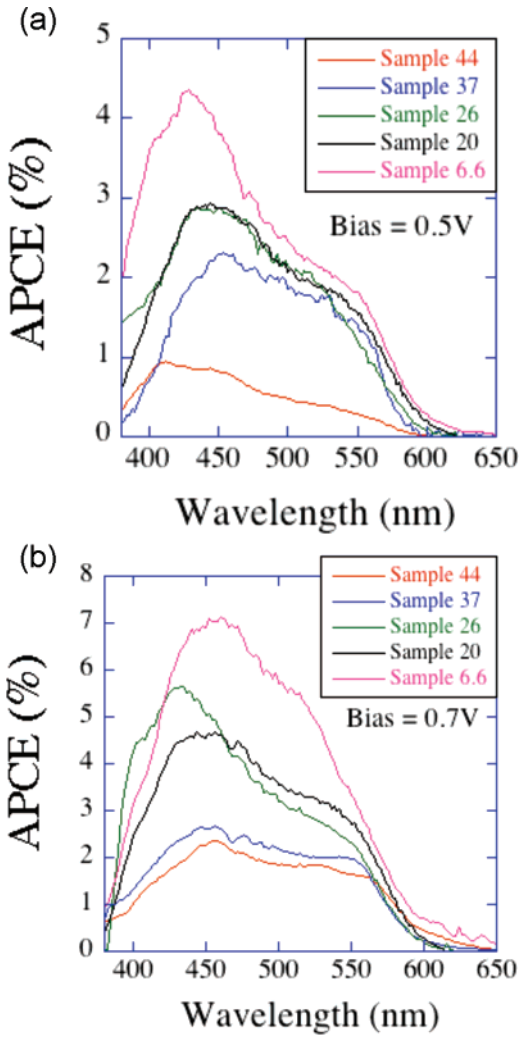

Figure 10. Absorbed photon-to-current efficiency (APCE) of Ti−Fe−O nanotube array samples at: (a) 0.5 V bias, and (b) 0.7 V bias.

Acknowledgment. Support of this work by the Department of Energy under grant DE-FG02-06ER15772 is gratefully acknowledged. We acknowledge and appreciate the assistance of Vince Bojan, William R. Drawl, and Joe Kulick of the Penn State Materials Characterization Laboratories. We thank the reviewers for their helpful comments and suggestions.

References

(1) Fujishima, A.; Honda, M. *Nature* **1972**, *238*, 37.
(2) Aroutiounian, V. M.; Arakelyan, V. M.; Shannazaryan, G. E.; Stepanyan, G. M.; Turner, J. A.; Khaselev, O. *Int. J. Hydrogen Energy* **2002**, *27*, 33.
(3) Beerman, N.; Vayssieres, L.; Lindquist, S.-Eric; Hagfield, A. *J. Electrochem. Soc.* **2000**, *147*, 2456.
(4) Morin, F. J. *Phys. Rev.* **1954**, *93*, 1195.
(5) Gardner, R. F. G.; Sweett, F.; Tanner, D. W. *J. Phys. Chem. Solids* **1963**, *24*, 1183.
(6) Sato, N. *Electrochemistry at Metal and Semiconductor Electrodes*; Elsevier: Amsterdam, 1998; p 34.

(7) Murphy, A. B.; Barnes, P. R. F.; Randeniya, L. K.; Plumb, I. C.; Grey, I. E.; Horne, M. D.; Glasscock, J. A. *Int. J. Hydrogen Energy* **2006**, *31*, 1999.
(8) Grätzel, M. *Nature* **2001**, *414*, 338.
(9) Anpo, M.; Takeuchi, M.; Ikeue, K.; Dohshi, S. *Curr. Opin. Solid State Mater. Sci.* **2002**, *6*, 381.
(10) Yamashita, H.; Harada, M.; Misaka, J.; Takeuchi, M.; Neppolian, B.; Anpo, M. *Catal. Today* **2003**, *84*, 191.
(11) Klosek, S.; Raftery, D. *J. Phys. Chem. B* **2001**, *105*, 2815.
(12) Iketani, K.; Hirota, K.; Yamaguchi, O.; Sun, R.-D.; Toki, M. *Mater. Sci. Eng. B* **2004**, *108*, 187.
(13) Liu, G. G.; Zhang, X. Z.; Xu, Y. J.; Niu, X. S.; Zheng, L. Q.; Ding, X. J. *Chemosphere* **2004**, *55*, 1287.
(14) Sung-Suh, H. M.; Choi, J. R.; Hah, H. J.; Koo, S. M.; Bae, Y. C.; *J. Photochem. Photobiol., A* **2004**, *163*, 37.
(15) Li, X.; Yue, P.-L.; Kutal, C. *New J. Chem.* **2003**, *27*, 1264.
(16) Nagaveni, K.; Hegde, M. S.; Madras, G. *J. Phys. Chem. B* **2004**, *108*, 20204.
(17) Gracia, F.; Holgado, J. P.; Caballero, A.; Gonzales-Elipe, A. R. *J. Phys. Chem. B* **2004**, *108*, 17466.
(18) Serpone, N.; Lawless, D.; Disdier, J.; Herrmann, J.-M. *Langmuir* **1994**, *10*, 643.
(19) Kennedy, J. H.; Frese, J. K. W. *J. Electrochem. Soc.* **1978**, *125*, 709.
(20) Gong, D.; Grimes, C. A.; Varghese, O. K.; Hu, W.; Singh, R. S.; Chen, Z.; Dickey, E. C. *J. Mater. Res.* **2001**, *16*, 3331.
(21) Paulose, M.; Shankar, K.; Yoriya, S.; Prakasam, H. E.; Varghese, O. K.; Mor, G. K.; Latempa, T. J.; Fitzgerald, A.; Grimes, C. A. *J. Phys. Chem. B* **2006**, *110*, 16179.
(22) Prakasam, H. E.; Shankar, K.; Paulose, M.; Grimes, C. A. *J. Phys. Chem. C* **2007**, *111*, 7235.
(23) Shankar, K.; Mor, G. K.; Fitzgerald, A.; Grimes, C. A. *J. Phys. Chem. C* **2007**, *111*, 21.
(24) Frank, A. J.; Kopidakis, N.; van de Lagemaat, J. *Coord. Chem. Rev.* **2004**, *248*, 1165.
(25) Paulose, M.; Varghese, O. K.; Mor, G. K.; Grimes, C. A.; Ong, K. G. *Nanotechnology* **2006**, 17, 398. Varghese, O. K.; Yang, X.; Kendig, J.; Paulose, M.; Zeng, K.; Palmer, C.; Ong, K. G.; Grimes, C. A. *Sens. Lett.* **2006**, *4*, 120.
(26) Varghese, O. K.; Gong, D.; Paulose, M.; Ong, K. G.; Grimes, C. A. *Sens. Actuators, B* **2003**, *93*, 338. Varghese, O. K.; Mor, G. K.; Grimes, C. A.; Paulose, M.; Mukherjee, N. *J. Nanosci. Nanotechnol.* **2004**, *4*, 733.
(27) Mor, G. K.; Varghese, O. K.; Paulose, M.; Grimes, C. A. *Sens. Lett.* **2003**, *1*, 42.
(28) Mor, G. K.; Carvalho, M. A.; Varghese, O. K.; Paulose, M.; Pishko, M. V.; Grimes, C. A. *J. Mater. Res.* **2004**, *19*, 628.
(29) Albu, S. P.; Ghicov, A.; Macak, J. M.; Hahn, R.; Schmuki, P. *Nano Lett.* **2007**, *7*, 1286.
(30) Mor, G. K.; Shankar, K.; Paulose, M.; Varghese, O. K.; Grimes, C. A. *Nano Lett.* **2006**, *6*, 215.
(31) Zhu, K.; Neale, N. R.; Miedaner, A.; Frank, A. J. *Nano Lett.* **2007**, *7*, 69.
(32) Mor, G. K.; Shankar, K.; Paulose, M.; Varghese, O. K.; Grimes, C. A. *Nano Lett.* **2005**, *5*, 191.
(33) Varghese, O. K.; Paulose, M.; Shankar, K.; Mor, G. K.; Grimes, C. A. *J. Nanosci. Nanotechnol.* **2005**, *5*, 1158.
(34) Mor, G. K.; Varghese, O. K.; Paulose, M.; Grimes, C. A. *Adv. Funct. Mater.* **2005**, *15*, 1291.
(35) Mor, G. K.; Varghese, O. K.; Paulose, M.; Mukherjee, N.; Grimes, C. A. *J. Mater. Res.* **2003**, *18*, 2588.
(36) Cai, Q.; Paulose, M.; Varghese, O. K.; Grimes, C. A. *J. Mater. Res.* **2005**, *20*, 230.
(37) Mor, G. K.; Varghese, O. K.; Paulose, M.; Shankar, K.; Grimes, C. A. *Sol. Energy Mater. Sol. Cells* **2006**, *90*, 2011.
(38) Feng, X.; Macak, J. M.; Schmuki, P. *Chem. Mater.* **2007**, *19*, 1534.
(39) Yoriya, S.; Prakasam, H. E.; Varghese, O. K.; Shankar, K.; Paulose, M.; Mor, G. K.; Latempa, T. J.; Grimes, C. A. *Sens. Lett.* **2006**, *4*, 334.
(40) Shankar, K.; Mor, G. K.; Prakasam, H. E.; Yoriya, S.; Paulose, M.; Varghese, O. K.; Grimes, C. A. *Nanotechnology* **2007**, *18*, 065707.
(41) Prakasam, H. E.; Varghese, O. K.; Paulose, M.; Mor, G. K.; Grimes, C. A. *Nanotechnology* **2006**, *17*, 4285.
(42) Varghese, O. K.; Grimes, C. A. *J. Nanosci. Nanotechnol.* **2003**, *3*, 277.
(43) Melody, B.; Kinard, T.; Lessner, P. *Electrochem. Solid-State Lett.* **1998**, *1*, 126.
(44) Krembs, G. M. *J. Electrochem. Soc.* **1963**, *110*, 938.
(45) Li, Y. M.; Young, L. *J. Electrochem. Soc.* **2001**, *148*, B337.
(46) Lu, Q.; Hashimoto, T.; Skeldon, P.; Thompson, G. E.; Habazaki, H.; Shimizu, K. *Electrochem. Solid-State Lett.* **2005**, *8*, B17.
(47) Varghese, O. K.; Paulose, M.; Gong, D.; Grimes, C. A.; Dickey, E. C. *J. Mater. Res.* **2003**, *18*, 156.
(48) Gennari, F. C.; Pasquevich, D. M. *J. Mater. Sci.* **1998**, *33*, 1571.
(49) Shannon, R. D.; Pask, J. A. *J. Am. Ceram. Soc.* **1965**, *48*, 391.
(50) Wang, R.; Sakai, R.; Fujishima, A.; Watanabe, T.; Hashimoto, K. *J. Phys. Chem. B* **1999**, *103*, 2188.
(51) Dghoughi, L.; Elidrissi, B.; Bernède, C.; Addou, M.; Lamrani, M. A.; Regragui, M.; Erguig, H. *Appl. Surf. Sci.* **2006**, *253*, 1823.
(52) Ozer, N.; Tepehan, F. *Solar Energy Sol. Cells* **1999**, *56*, 141.
(53) Schneider, J. J.; Czap, N.; Hagen, J.; Engstler, J.; Ensling, J.; Gutlich, P.; Reinoehl, U.; Bertagnolli, H.; Luis, F.; Jongh, L. J. de; Wark, M.; Grubert, G.; Hornyak, G. L.; Zanoni, R. *Chem.—Eur. J.* **2000**, *6*, 4305.
(54) Gracia, F.; Holgado, J. P.; Yubero, F.; González-Elipe, A. R. *Surf. Coat. Technol.* **2002**, *158−159*, 552.
(55) Grosvenor, A. P.; Kobe, B. A.; Biesinger, M. C.; McIntyre, N. S. *Surf. Interface Anal.* **2004**, *36*, 1564.
(56) Heimer, T. A.; Heilweil, E. J.; Bignozzi, C. A.; Meyer, G. J. *J. Phys. Chem. A* **2000**, *104*, 4256.
(57) Kay, A.; Cesar, I.; Gratzel, M. *J. Am. Chem. Soc.* **2006**, *128*, 15714.
(58) Grimes, C. A. *J. Mater. Chem.* **2007**, *17*, 1451.

NL0710046